Matter

Article

Quantum confinement effects in the topological Dirac semimetal α-Sn on InSb(111)

Graphical abstract

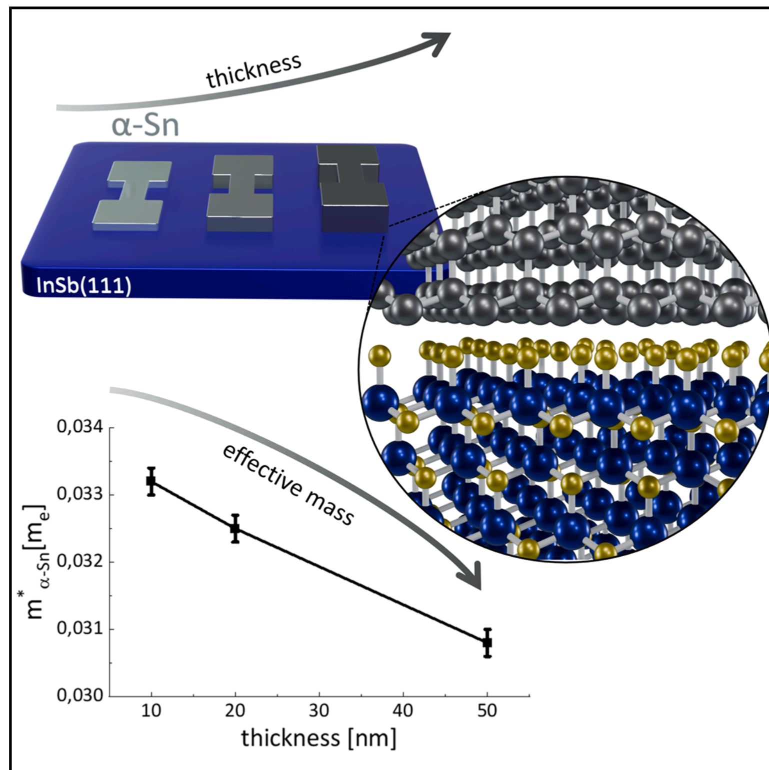

Highlights

- The topological properties of α-Sn can be tuned by the in-plane strain
- Epitaxial growth of α-Sn on InSb(111) induces a topological Dirac semimetal phase
- Quantum confinement effects in thin α-Sn films on InSb(111) are investigated
- Thickness-dependent electrical transport and effective masses are observed

Authors

Chiara Massetti, Carolina Crosta, Florian Le Mardelé, ..., Milan Orlita, Carlo Grazianetti, Fabio Pezzoli

Correspondence

carlo.grazianetti@cnr.it (C.G.),
fabio.pezzoli@unimib.it (F.P.)

In brief

The application of a compressive strain on α-Sn turned out to induce a topological Dirac semimetal phase (i.e., a three-dimensional graphene-like dispersion of the bands) that can be easily obtained by the epitaxial growth on the slightly mismatched InSb(111) substrate. Quantum confinement effects on thin α-Sn films reveal a thickness-dependent electrical transport and the change in the effective masses of the charge carriers. These findings are insightful regarding the potential applications in next-generation quantum devices.

Demonstrate
Proof-of-concept of performance with intended application/response

Massetti et al., 2025, Matter *8*, 102194
September 3, 2025 © 2025 The Author(s).
Published by Elsevier Inc.
https://doi.org/10.1016/j.matt.2025.102194

CellPress

Matter

Article

Quantum confinement effects in the topological Dirac semimetal α-Sn on InSb(111)

Chiara Massetti,[1] Carolina Crosta,[2] Florian Le Mardelé,[3] Ivan Mohelský,[3] Christian Martella,[1] Alessandro Molle,[1] Milan Orlita,[3,4] Carlo Grazianetti,[1,*] and Fabio Pezzoli[2,5,*]

[1]CNR-IMM Agrate Brianza Unit, Via C. Olivetti 2, 20864 Agrate Brianza, Italy
[2]Dipartimento di Scienza dei Materiali, Università degli Studi di Milano-Bicocca, BiQuTe, Via Cozzi 55, 20125 Milan, Italy
[3]Laboratoire National des Champs Magnétiques Intenses-European Magnetic Field Laboratory (LNCMI-EMFL), CNRS UPR3228, University Grenoble Alpes, Grenoble, France
[4]Faculty of Mathematics and Physics, Charles University, Ke Karlovu 5, 121 16 Prague, Czech Republic
[5]Lead contact
*Correspondence: carlo.grazianetti@cnr.it (C.G.), fabio.pezzoli@unimib.it (F.P.)
https://doi.org/10.1016/j.matt.2025.102194

PROGRESS AND POTENTIAL Stimulated by recent discoveries in topology, renewed interest in α-Sn, a diamond-like allotrope of tin, makes this single-element material a promising candidate for quantum applications. By inducing the topological Dirac semimetal phase through epitaxial strain on the InSb(111) substrate, we have explored the influence of quantum confinement on its electronic structure. The electrical transport characterization, together with the cyclotron resonance analysis, reveal a thickness-dependent modification of transport mechanisms and effective mass, shedding light on the intricate interplay between quantum confinement and topological properties. These findings enhance the fundamental understanding of α-Sn nontrivial electronic properties and provide a solid foundation for its integration into next-generation electronic and quantum devices. With further advancements in growth techniques and device engineering, α-Sn could play a crucial role in the development of energy-efficient, high-performance technologies beyond the current state of the art.

SUMMARY

The diamond-like allotrope of Sn (α-Sn) is tantalizing, being an elemental semimetal that hosts a range of topological properties. Despite the intriguing potential of this quantum material, a detailed understanding of its nontrivial electronic structure remains relatively poor. Here, we prepared α-Sn in a well-defined quantum phase (i.e., topological Dirac semimetal) by applying a compressive strain via epitaxial growth on the (111) surface of an InSb substrate. We varied the thickness of the α-Sn epilayer to single out the emergence of quantum confinement effects. Our electrical investigation suggests a thickness-dependent modification of transport mechanisms. These results are complemented by the measurement of the cyclotron resonance, which manifests the role of quantum confinement in defining the effective mass of topological Dirac fermions as bulk carriers. Our results contribute to deepening the knowledge of the α-Sn electronic properties. This is pivotal to increase the future applicability of Sn-based architectures into beyond-state-of-the-art devices.

INTRODUCTION

Although largely studied in the past,[1–4] the interest in α-Sn, a diamond-like allotrope of Sn, has been renewed after the discoveries of the topological properties of matter and the realization of a Sn-based graphene-like lattice called stanene.[5,6] In this framework, α-Sn is one of the most promising and especially attractive candidates in the field of topological materials, due to the presence of various quantum phases that are tunable via materials properties such as thickness, strain, and alloying or by applying external electromagnetic fields.[7,8] Sn has a large atomic number compared with the other lighter group IV companions, such as carbon, silicon, and germanium. This characteristic is reflected in a sizable contribution of the spin-orbit coupling that generates an inversion of the order between the light hole (LH) and the s-like conduction band.[9,10] Unstrained, bulk α-Sn is thus a semimetal with a zero gap protected by the cubic symmetry of the crystal, but a non-trivial topological character can be induced upon external perturbations.[8,11–16] Epitaxy on a non-commensurate substrate is one of the

© 2025 The Author(s). Published by Elsevier Inc.
This is an open access article under the CC BY-NC-ND license (http://creativecommons.org/licenses/by-nc-nd/4.0/).

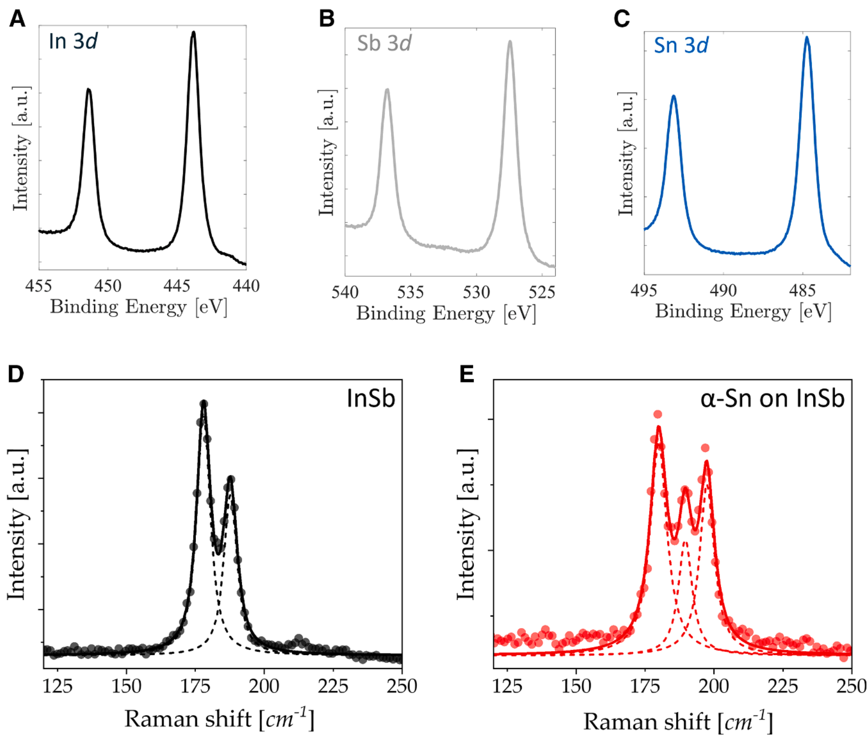

Figure 1. *In situ* and *ex situ* characterizations before and after α-Sn growth

(A–C) XPS core levels of (A) In 3*d*, (B) Sb 3*d*, and (C) Sn 3*d*, respectively. The In and Sb 3*d* core levels are acquired before the growth of 10-nm-thick α-Sn film and the Sn 3*d* after growth.

(D and E) Raman spectra of (D) a bare InSb substrate and (E) a 10-nm-thick α-Sn/InSb heterojunction. The raw data are the scattered points, the solid curve is the corresponding fit result, while the dashed lines show the individual spectral components used in the fitting procedure.

See also Figure S2.

conventional strategies to reduce the lattice symmetry, as reported for instance in the growth of the Xenes beyond graphene.[17] Owing to the distortion of the Sn lattice, the strain-induced modification of the physical properties provides an effective means to tailor the electronic structure and the quantum phase.

Specifically, in the case of a compressive strain, α-Sn turns out to be a three-dimensional (3D) topological Dirac semimetal (TDS), whereas a tensile strain yields a 3D topological insulator (TI).[18–20] In other words, strain can develop either negative or positive energy gaps, when it is compressive or tensile, respectively.[10] Lately, epitaxial growth of thin films of α-Sn has been reported on the (001) and (111) surfaces of both InSb and CdTe substrates, mostly through molecular beam epitaxy (MBE).[3,10,19,21] Previous works[19] suggested that the lattice mismatch between Sn[22] and InSb[23] results in the growth of the TDS phase for α-Sn owing to the in-plane compressive strain of about $\varepsilon_{\parallel} \sim -0.14\%$. The latter induces a small (negative) gap of ~10–20 meV at the Γ point, splitting the single-point Fermi surface into two points—still remaining a semimetal but with a different dispersion (i.e., linear in all three momentum directions thus being characteristic of a TDS phase) (see Figure S1 for theoretical calculations within the 8-band $k{\cdot}p$ framework[24]). However, crucial information related to the emergence of quantum confinement effects in the novel (111)-oriented TDS growth is still lacking, despite its additional potential to enable the deposition of α-Sn in the 2D stanene limit.[19,25] In this work, we fill this knowledge gap by conducting thickness-dependent investigations through electrical and magneto-optical measurements of thin films grown directly on InSb(111) substrates, whose thickness of α-Sn was varied between 5 and 50 nm.

RESULTS AND DISCUSSION

α-Sn is deposited through MBE at room temperature on undoped Sb-terminated InSb(111) substrate (see methods). Before the Sn growth, the InSb substrate is investigated through *in situ* X-ray photoelectron spectroscopy (XPS). In Figures 1A and 1B, the 3*d* core levels of In and Sb are respectively shown. After the Sn growth (10 nm), the Sn 3*d* core levels (placed in between In 3*d* and Sb 3*d*) are also observed, as shown in Figure 1C. The spin-orbit separations between the $d_{5/2}$ and $d_{3/2}$ components are equal to $\Delta_{3d}^{In} = 7.55$ eV, $\Delta_{3d}^{Sb} = 9.37$ eV, and $\Delta_{3d}^{Sn} = 8.40$ eV.

Figures 1D and 1E show the Raman spectroscopy characterization before and after the deposition of a 10-nm-thick Sn film (see also Figure S2, showing the homogeneity of α-Sn deposition over the sample sizes). The InSb substrate exhibits two Raman modes at ~180 and 190 cm^{-1} due to the transverse and longitudinal optical modes, respectively,[26] while α-Sn is characterized by a 1Γ mode centered around 197 cm^{-1}.[2,27]

In the following, we address the transport properties of α-Sn. Different epilayer thicknesses have been characterized (5, 10, and 20 nm) using the single-channel structure schematized in Figures 2A and 2B (see methods for details). The devices have been analyzed by measuring the current-voltage curves in the 77–300 K range. Figures 2C–2E demonstrate the resulting temperature-dependent resistance, R(T), obtained for the three different thicknesses.

It is worth noting that as the lattice temperature approaches 300 K, the intrinsic carrier concentration promoted in the substrate can become sizable (e.g., ~10^{16} cm^{-3}),[28] thus offering a preferential conductive channel for the current flowing in the heterostructure. This consideration leads to the natural assumption that the high-temperature R(T) characteristic is expected to be governed mostly by the highest resistive component of the device (i.e., the α-Sn film) and to a negligible current through such epitaxial layers, compared to that flowing via the substrate. Such peculiar behavior can offer a convenient opportunity to gather instrumental access to the inherent properties of the TDS itself. To scrutinize this possibility, we begin by noticing that all the R(T) curves of Figure 2 feature a bell-shaped profile with a maximum around 150 K. This is such a puzzling

CellPress
OPEN ACCESS

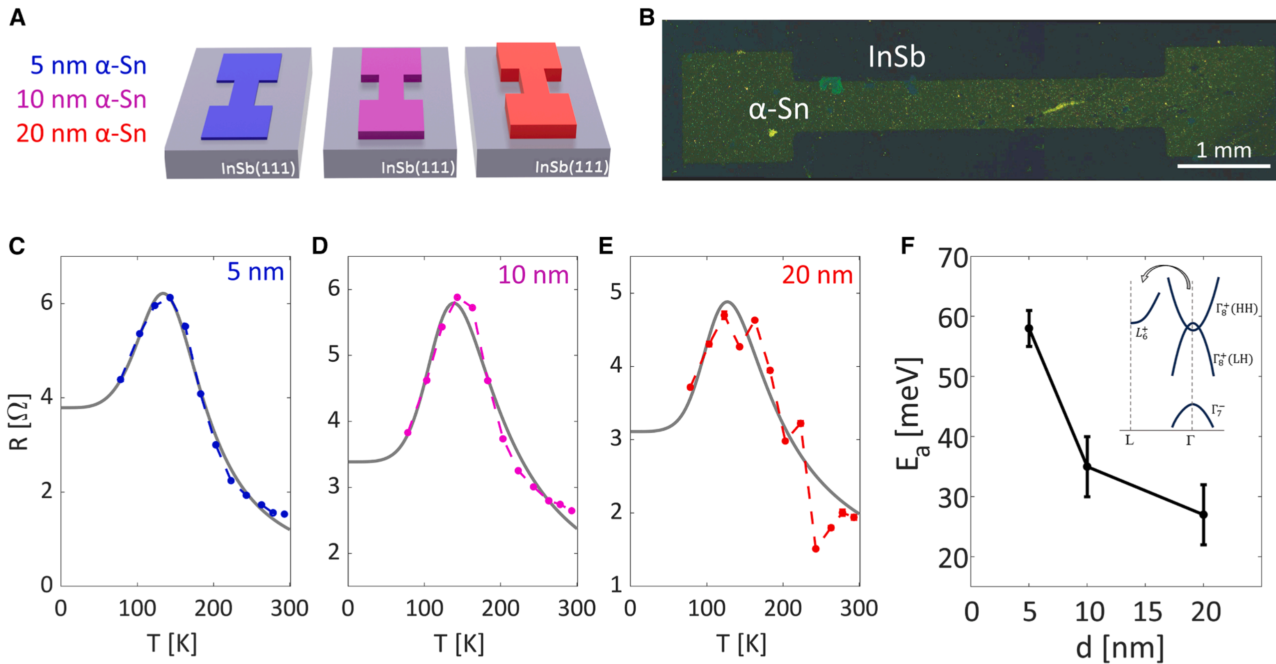

Figure 2. Electrical transport in the α-Sn thin films on InSb(111)

(A) Sketch of the single-channel structures patterned for the electrical characterization of α-Sn of 5-, 10-, and 20-nm thicknesses.

(B) Optical image of the 20-nm-thick single-channel structure.

(C–E) R(T) curves obtained for α-Sn samples with thicknesses of (C) 5 nm, (D) 10 nm, and (E) 20 nm.

(F) Evolution of energy activation as a function of Sn film thickness. The inset shows the schematic band structure of α-Sn, and the arrow highlights the transition from Γ- to L-valley.

See also Figures S3 and S5 and Tables S1 and S2.

dependence, which is also found for other topological materials.[29,30] However, it differs from the monotonic behavior observed in the InSb(111) substrate (see Figure S3) and from recent literature data for α-Sn grown on CdTe(001), where resistivity dependence on temperature was shown to radically change when the α-Sn thickness was reduced from 100 to 10 nm.[31]

As suggested in the literature, the resistive behavior observed in Figures 2C–2E for α-Sn on InSb(111) stems from intertwined contributions originating from the multi-valley nature of the band structure of this TDS and is likely affected by the temperature-dependent populations and effective masses of L-valley electrons, LHs, and heavy holes.[21,31–33] Such an interpretation is further corroborated by an analytical calculation of the Fermi-Dirac distribution of the carrier densities (see Figure S4) recently introduced.[34] In the intrinsic regime (i.e., high-temperature range ∼300 K), electrons are effectively promoted from the Dirac cone to in the L-valleys via intervalley scattering, and concomitantly the hole concentration increases. Upon cooling below room temperature, carriers are expected to freeze out toward the Dirac cone as a result of a progressive depopulation of the thermally excited L-valley electrons, yielding a net increase of the device resistance.[31] The semiconductor-like behavior, $R_s(T)$, established as the temperature approaches 150 K, can thus be regarded as a manifestation of the activation energy between states at the center (Γ-valley) and the edge (L-valley) of the Brillouin zone.[21,31–33]

The competition between carrier population and effective masses further emerges as the temperature is additionally reduced below the critical value of about 150 K. In this case, previous works have demonstrated that the marked resistance decrease seen in Figures 2C–2E can likely occur because charge transport is progressively dominated by high-mobility Γ-valley carriers, and a metal-like character $R_m(T)$ sets in.[31,35]

Following previous literature results, we can approximate the temperature-induced changes of the resistance as[21,33]

$$\frac{1}{R(T)} = \frac{1}{R_s(T)} + \frac{1}{R_m(T)}. \qquad \text{(Equation 1)}$$

While this analysis is overly simplified, as it neglects various processes (e.g., impurity and intervalley scattering at low temperatures), it is nevertheless suited to quickly glance the possible emergence of quantum confinement effects. Indeed, despite being qualitative, this approach can be useful specifically in the high-temperature regime. As argued in the literature,[21,33] the resistive behavior can be singled out using the following Arrhenius law:[36]

$$R_s(T) = R_\infty e^{E_a/k_B T} \qquad \text{(Equation 2)}$$

where k_B is the Boltzmann constant, R_∞ is the resistance at very high temperatures, and E_a is an activation energy. Conversely,

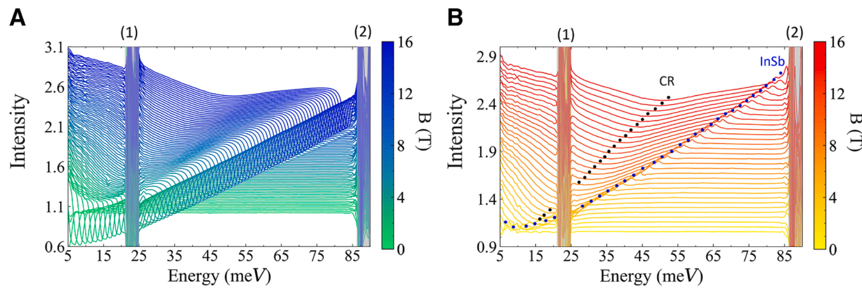

Figure 3. Magneto-optical characterization of 20-nm-thick α-Sn

(A) Relative magneto-transmission spectra, $T_s(B)/T_s(0)$, collected at T = 4.2 K on the 20-nm-thick sample for selected values of the applied magnetic field (the offset in vertically stacking scales with B).

(B) The magneto-optical data from (A) normalized by the relative magneto-transmission of the bare InSb substrate: $T_{ref}(B)/T_{ref}(0)$—in other words, $[T_s(B)/T_s(0)]/[T_{ref}(B)/T_{ref}(0)]$. The black dots indicate the position of the CR dip, while blue dots highlight the remaining signal from the InSb substrate. The areas (1) and (2) in both panels correspond, respectively, to the spectral region fully opaque due to the Reststrahlen band of InSb and absorption in the beamsplitter.

the low-temperature component can be simplified by assuming a dependence like[37]

$$\frac{1}{R_m(T) - R(0)} = \frac{1}{C_1 T^n} + \frac{1}{C_2 T} \qquad \text{(Equation 3)}$$

where C_1 and C_2 are related to the two distinct transport regimes depending on the phonon system degeneracy, while $R(0)$ is the resistance in the limit of temperature of 0 K, in which scattering from defects is present among the other effects. It is interesting to note that the value of the exponent n has been associated in the literature with 3D- or 2D-like transport, owing to a T^5 or T^4 scaling dependence, respectively.[37,38] As shown in Figures 2C–2E, each R(T) curve is nicely fitted by the simple two-regime model.

The data reduction, summarized in Table S1, possibly suggests that the T^4 dependence is slightly favorable compared to the T^5 scaling only for the 5-nm-thick sample, thus indicating that at cryogenic temperatures and in this low-thickness regime, the conduction might possibly occur thanks to the emergence of 2D gas. It should be noted, however, that given the limitations of the model in the low-temperature regime, and the close χ^2 similarity between the $n = 4$ and $n = 5$ scaling (see Tables S1 and S2), as also reported for α-Sn on Si[33] or CdTe,[21] further investigation is needed to better address such a behavior.

The modeling discloses another remarkable effect of the epilayer thickness when we consider the thermal excitation of carriers in the high-temperature range. The values of the Γ-L energy activation, extrapolated from the R(T) data above 150 K, are summarized in Figure 2F for the various samples. It can be noted that a drastic increase in the amplitude of the thermal gap takes place as the epilayer thickness decreases. Similarly, the peak resistance scales with the film thickness (see Figure S3). All these findings further support the assumption of the negligible contribution of the substrate in the resistance measurement because the bulk InSb, being the same wafer for all the epitaxial layers, would have yielded a constant E_a value, if any. As an additional control experiment, we have repeated the growth of the 20-nm-thick α-Sn film deposited on a different InSb(111) wafer using a second MBE apparatus. The temperature-dependent resistance was found to be in good agreement with the previous set of data (see Figure S5), demonstrating reproducibility and confirming the primary role of the TDS layer in defining the measured current-voltage characteristic of the device. Such a finding provides striking evidence for the emergence of quantum-size effects in the conduction of α-Sn/InSb(111).[21,39]

To gain a more quantitative understanding of conduction mechanisms, particularly at the Γ-valley, and to provide useful information about the impact of quantum confinement on the electronic properties of the TDS in the 3D regime, we measured the low-temperature absorption in the far-infrared (IR), focusing on as-grown α-Sn films thicker than 5 nm, namely 10, 20, and 50 nm. Notably, the application of high magnetic fields (see methods) yields cyclotron resonances (CRs) and enables the contactless determination of the effective mass of the carriers, which proved effective in both single crystals and thin films.[40] To better disclose the field-induced changes in the optical response of the samples, the transmission (T) measured at a given magnetic field (B) is normalized, unless otherwise noted, by the zero-field spectrum (i.e., $T_s(B)/T_s(0)$). This quantity is referred to as relative magneto-transmission (Figures 3A and 4A–4C).

The spectra of the 20-nm-thick sample are presented in Figure 3A as a vertically stacked plot. The intensity of the normalized transmission is reported as a function of the incident radiation energy in the 0 to 100 meV range. Two spectrally narrow regions are dominated by noise (marked in gray in Figure 3A) that is due either to the absorption associated to the Reststrahlen band of the InSb substrate[41] (area 1 between 21 and 25 meV) or to instrumental optical losses at the beamsplitter of the interferometer (area 2 between 86 and 93 meV). The dominant feature emerging in the normalized magneto-transmission data of Figure 3A is a pronounced dip that at B = 1 T is around 8.8 meV and progressively blueshifts with the field.[42,43]

This line is also well seen in Figures 4A–4C, where we report the same set of data in the form of a false-color plot for all three samples investigated. This line is easily identified as cyclotron resonance of bulk electrons in bulk InSb.[44,45] To enhance the signal from the α-Sn layer, we have also used an alternative way of plotting our magneto-optical data—that is, substrate-normalized magneto-transmission. This corresponds to relative magneto-transmission of the sample, $T_s(B)/T_s(0)$, additionally normalized by relative magneto-transmission of the bare InSb substrate, $T_{ref}(B)/T_{ref}(0)$. Special care was taken to ensure reproducibility by performing measurements of the α-Sn films and of the InSb(111) reference using the same acquisition parameters. These substrate-normalized data are shown in Figures 3B and 4D–4F. Additional plots demonstrating the

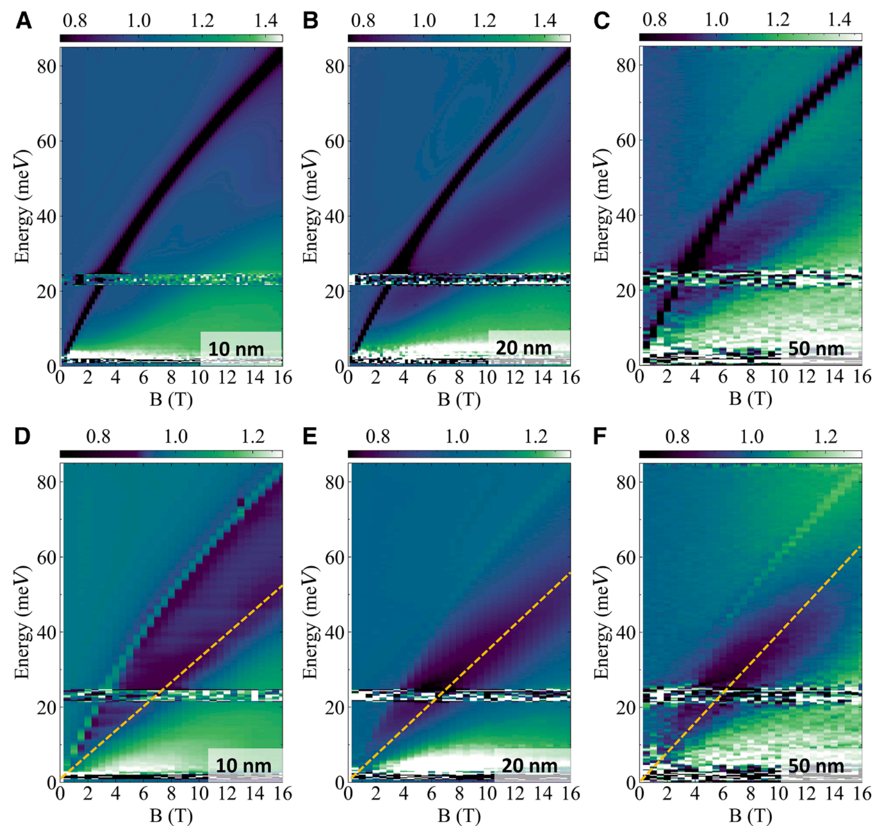

Figure 4. Normalization comparison of magneto-transmission maps for different α-Sn thicknesses

False-color maps of relative magneto-transmission, $T_s(B)/T_s(0)$, collected on α-Sn samples with the thicknesses of (A) 10 nm, (B) 20 nm, and (C) 50 nm. For comparison, and to enhance the CR from α-Sn layers, we also plot the same set of data with additional normalization by relative magneto-transmission of the bare InSb substrate in (D)–(F), respectively. The yellow dashed lines highlight the CR line in the α-Sn films.

See also Figures S6 and S7.

Such data represent the first estimate of the effective masses for α-Sn directly grown on InSb(111). We can nevertheless find reassurance of their validity and consistency with TDS conduction[47] via the 3D conical Dirac bands by considering that they are in line with the literature data for thick films of strained α-Sn grown on CdTe(001)[48,49] and on InSb(001)[50] substrates.

It is worth noting, however, that the compelling modification of the effective mass emerging from the magneto-absorption measurements can be interpreted in the framework of Kane's formalisms[51,52] as a result of a quantization gap in trivial semiconductors.[10] Such findings confirm the occurrence of quantum confinement effects and might be linked to the 2D-to-3D crossover suggested by the resistance data below 10 nm.

While anisotropy in the dispersion of the Dirac bands can also contribute to the observed effective mass variation, it is interesting to note that theoretical predictions[39,53,54] and experimental reports,[10,55] primarily in prototypical materials such as Cd_3As_2, support the conclusions by suggesting that compressively strained α-Sn confined to a reduced thickness can sustain a quantum phase transition from a TDS to a TI, the latter being characterized by a large band gap and high mobility carriers, such as those shown here.[47] However, further studies are needed to clarify such a possibility.

frequency derivative of magneto-transmission are presented in Figures S6A–S6C, together with magneto-transmission of the bare InSb substrate in Figures S7A and S7B. Importantly, a closer look at Figures 4A–4C reveals an additional excitation that appears solely in the epilayers in the energy window located below the InSb CR line. Even though characterized by a significantly weaker integral intensity, as compared to the InSb CR line, it is clearly present in all three investigated samples.

The resulting color-coded maps for all the samples are summarized in Figures 4D–4F. The corresponding spectra for the 20-nm-thick sample have been also vertically stacked in Figure 3B for further clarity. Despite the InSb line not being completely removed, a rather broad absorption feature, highlighted by the yellow dotted line in Figures 4D–4F, becomes better resolved. We ascribe it to the cyclotron resonance caused by mobile bulk carriers located at the Γ-valley of the α-Sn film. Since the cyclotron frequency is given by[46]

$$f_c = \frac{eB}{2\pi m^*}$$

where e is the electron charge and m^* is the effective mass, the transmission minima at the resonance lines, summarized in Figures 5A–5C, provide us with the effective masses. The thickness-induced change in m^* is reported in Figure 5D, demonstrating that the TDS transport is governed by carriers that become progressively lighter as the α-Sn thickness increases.

Conclusions

We investigated the thickness-dependent properties of α-Sn films grown on InSb(111). The temperature-dependent resistance clearly revealed the onset of quantum confinement effects. A complementary magneto-optical investigation confirmed this observation, also demonstrating a progressive decrease in the effective mass. The latter result is in line with the confinement-induced phenomena reported in other prototypical TDSs such Cd_3As_2[55] and Na_3Bi.[56] It is worth noting that the effective masses disclosed in α-Sn/InSb(111) are lower than in other TDSs,[55,57] making α-Sn additionally appealing in topological electronics, in light of its easier growth (at room temperature) because it is a single-element material.

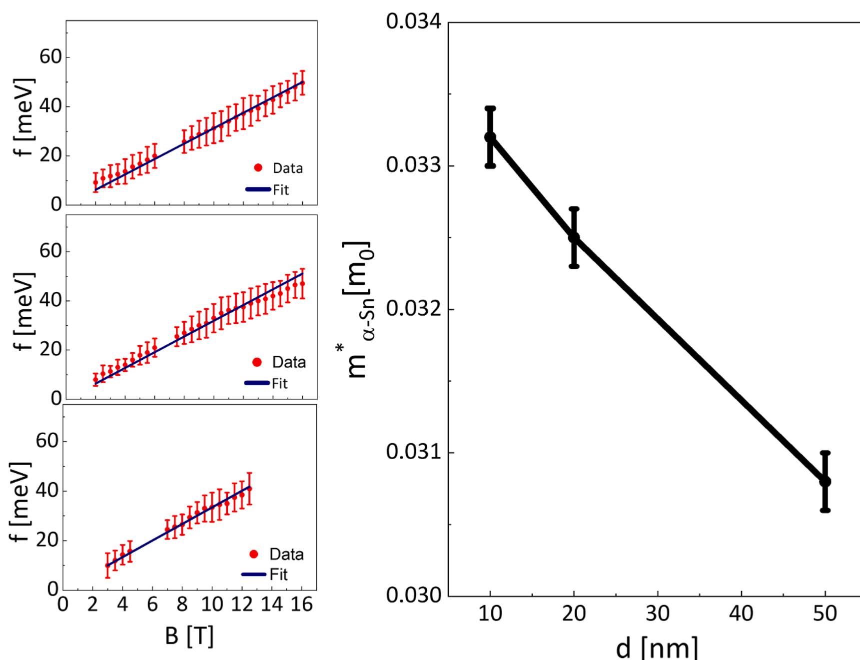

Figure 5. Extrapolation of effective masses for different thicknesses of α-Sn

(A–C) Linear fit of the CR frequency dip positions as a function of the magnetic field B for (A) 10 nm, (B) 20 nm, and (C) 50 nm of α-Sn thickness.

(D) Values of the effective mass extrapolated by the linear fitting of the cyclotron resonance lines, expressed in free electron mass (m_0) units, as a function of the α-Sn thickness.

METHODS

Growth and *in situ* characterization

The samples are grown in the MBE system with base pressure 10^{-10} mbar on undoped InSb(111) substrate. Before the growth, the substrate is prepared with several cycles of Ar^+ sputtering (1.5 kV) and annealing (at 330°C). Sn is evaporated at a rate of ∼2 Å/min to the desired thickness (between 5 and 50 nm), keeping the substrate at room temperature. Each sample is characterized by *in situ* XPS performed before and after the Sn growth. A non-monochromatized X-ray source (Mg anode, $h\nu$ = 1,253.6 eV) in surface-sensitive conditions (takeoff angle of 37°) has been used. After the sputtering and annealing cycles, the substrate is not oxidized, as evidenced by the presence of single spectral lines related to the elemental In and Sb without the presence of the oxide-related components at higher binding energies (see Figure 1).

Raman spectroscopy

Raman spectra have been acquired through a solid-state laser (514 nm) in a backscattering configuration, coupled to an optical microscope equipped with a 50× objective, using a laser power of 1 mW and collecting 3 accumulations with an exposure time of 10 s.

Sample processing

The Sn structures (consisting of a channel of 4 × 0.7 mm) were made by patterning the samples through optical lithography using the Tabletop Maskless Aligner μMLA from Heidelberg. The etching of Sn is performed through aqua regia, realized with a mixture of nitric acid (HNO_3) and hydrochloric acid (HCl), with a ratio of HNO_3:HCl = 1:3 and diluted 1:50 in H_2O, to obtain an etching rate of ∼20 nm/min.

Electrical characterization

For the electrical transport measurements, a microscope cryostat (Linkam HFS600E-PB4) has been used to study the resistance as a function of temperature. It includes two metal cryogenic tips that can be manually placed on the sample to make electrical contact by means of Ag paste. These are connected to a Keithley Source-Meter-Unit 2450, through which the voltage-current curve data can be recorded. The cryostat is cooled with liquid nitrogen and connected to the PC through software to control the temperature. Reference InSb substrate for electrical measurements (Figure S3) has been sputtered and annealed as those used for the Sn growth. All the InSb substrates come from the same 2-in wafer.

Magneto-optical characterization

The magneto-optical data were collected in transmission mode, using a globar as a broadband source of IR radiation, which was delivered to the sample via light-pipe optics and analyzed by a Fourier transform spectrometer. The experiment was performed at a temperature of 4.2 K in the Faraday configuration, which corresponds to the magnetic field parallel to the light wave vector. The available magnetic field ranged from 0 to 16 T and was delivered by a superconducting solenoid. The sample and bolometer, placed directly below the sample holder, were positioned in a sealed probe kept under low pressure, ensuring sufficient heat transfer with the He bath of the magnet cryostat.

RESOURCE AVAILABILITY

Lead contact

Requests for further information and resources should be directed to and will be fulfilled by the lead contact, Fabio Pezzoli (fabio.pezzoli@unimib.it).

Materials availability

This study did not generate new unique materials.

Data and code availability

- All data reported in this paper will be shared by the lead contact upon request.
- This paper does not report original code.
- Any additional information required to reanalyze the data reported in this paper is available from the lead contact upon request.

ACKNOWLEDGMENTS

We acknowledge E. Vitiello for technical assistance with the electrical measurements. This material is based upon work supported by the Air Force Office of Scientific Research under award no. FA8655-22-1-7050. This work was supported in part by European Union (EU) funding from the H2020 research and innovation programme under ERC-COG 2017 grant no. 772261 ''XFab'' and from the Horizon Europe Programme under the ERC-PoC 2022 grant no. 101069262 "XMem." C.G. and C. Martella acknowledge the financial support of the projects EMPEROR (grant no. 20225L4EBJ, CUP B53D23008560006) and DESIGN (grant no. 2022EE8KH9, CUP B53D23008770006), respectively. These projects received funding from the Italian Programme for Research Projects of Outstanding National Interest (PRIN) and Next Generation EU, under the National Recovery and Resilience Plan (NRRP), Mission 04, Component 2.

AUTHOR CONTRIBUTIONS

Conceptualization, C.G. and F.P. Formal analysis, C. Massetti, C.C., M.O., and F.P. Investigation, C. Massetti, C.C., F.L., I.M., C. Martella, M.O., C.G., and F. P. Writing, C. Massetti, C.G., and F.P. Supervision, A.M., M.O., C.G., and F.P. Funding acquisition, C. Martella, A.M., C.G., and F.P.

DECLARATION OF INTERESTS

The authors declare no competing interests.

SUPPLEMENTAL INFORMATION

Supplemental information can be found online at https://doi.org/10.1016/j.matt.2025.102194.

Received: August 7, 2024
Revised: February 14, 2025
Accepted: May 6, 2025
Published: May 30, 2025

REFERENCES

1. Price, D.L., and Rowe, J.M. (1969). The crystal dynamics of grey α-tin at 90°K. Solid State Commun. *7*, 1433–1438. https://doi.org/10.1016/0038-1098(69)90318-4.
2. Menéndez, J., and Höchst, H. (1984). Study of the phase transition in heteroepitaxially grown films of αSn by Raman spectroscopy. Thin Solid Films *111*, 375–379. https://doi.org/10.1016/0040-6090(84)90329-8.
3. Gómez, J.A., Guenzburger, D., Ellis, D.E., Hu, M.Y., Alp, E., Baggio-Saitovitch, E.M., Passamani, E.C., Ketterson, J.B., and Cho, S. (2003). Theoretical and experimental study of α-Sn deposited on CdTe(001). Phys. Rev. B *67*, 115340. https://doi.org/10.1103/PhysRevB.67.115340.
4. Ohtsubo, Y., Le Fèvre, P., Bertran, F., and Taleb-Ibrahimi, A. (2013). Dirac cone with helical spin polarization in ultrathin α-Sn(001) films. Phys. Rev. Lett. *111*, 1–5. https://doi.org/10.1103/PhysRevLett.111.216401.
5. Zhu, F.f., Chen, W.j., Xu, Y., Gao, C.l., Guan, D.d., Liu, C.h., Qian, D., Zhang, S.-C., and Jia, J.f. (2015). Epitaxial growth of two-dimensional stanene. Nat. Mater. *14*, 1020–1025. https://doi.org/10.1038/nmat4384.
6. Yuhara, J., Fujii, Y., Nishino, K., Isobe, N., Nakatake, M., Xian, L., Rubio, A., and Le Lay, G. (2018). Large area planar stanene epitaxially grown on Ag(1 1 1). 2D Mater. *5*, 025002. https://doi.org/10.1088/2053-1583/aa9ea0.
7. Ferrari, B.M., Marcantonio, F., Murphy-Armando, F., Virgilio, M., and Pezzoli, F. (2023). Quantum spin Hall phase in GeSn heterostructures on silicon. Phys. Rev. Res. *5*, L022035. https://doi.org/10.1103/PhysRevResearch.5.L022035.
8. Fu, L., and Kane, C.L. (2007). Topological insulators with inversion symmetry. Phys. Rev. B *76*, 045302. https://doi.org/10.1103/PhysRevB.76.045302.
9. Pollak, F.H., Cardona, M., Higginbotham, C.W., Herman, F., and Van Dyke, J.P. (1970). Energy-Band Structure and Optical Spectrum of Grey Tin. Phys. Rev. B *2*, 352–363. https://doi.org/10.1103/PhysRevB.2.352.
10. Anh, L.D., Takase, K., Chiba, T., Kota, Y., Takiguchi, K., and Tanaka, M. (2021). Elemental Topological Dirac Semimetal α-Sn with High Quantum Mobility. Adv. Mater. *33*, 2104645. https://doi.org/10.1002/adma.202104645.
11. Wang, X.-L., Dou, S.X., and Zhang, C. (2010). Zero-gap materials for future spintronics, electronics and optics. NPG Asia Mater. *2*, 31–38. https://doi.org/10.1038/asiamat.2010.7.
12. Barfuss, A., Dudy, L., Scholz, M.R., Roth, H., Höpfner, P., Blumenstein, C., Landolt, G., Dil, J.H., Plumb, N.C., Radovic, M., et al. (2013). Elemental Topological Insulator with Tunable Fermi Level: Strained α-Sn on InSb(001). Phys. Rev. Lett. *111*, 157205. https://doi.org/10.1103/PhysRevLett.111.157205.
13. Huang, H., and Liu, F. (2017). Tensile strained gray tin: Dirac semimetal for observing negative magnetoresistance with Shubnikov-de Haas oscillations. Phys. Rev. B *95*, 201101. https://doi.org/10.1103/PhysRevB.95.201101.
14. Zhang, D., Wang, H., Ruan, J., Yao, G., and Zhang, H. (2018). Engineering topological phases in the Luttinger semimetal α-Sn. Phys. Rev. B *97*, 195139. https://doi.org/10.1103/PhysRevB.97.195139.
15. Chen, K.H.M., Lin, K.Y., Lien, S.W., Huang, S.W., Cheng, C.K., Lin, H.Y., Hsu, C.-H., Chang, T.-R., Cheng, C.-M., Hong, M., and Kwo, J. (2022). Thickness-dependent topological phase transition and Rashba-like preformed topological surface states of \ensuremath{\alpha}-Sn(001) thin films on InSb(001). Phys. Rev. B *105*, 075109. https://doi.org/10.1103/PhysRevB.105.075109.
16. Khaetskii, A., Golovach, V., and Kiefer, A. (2022). Revisiting the physical origin and nature of surface states in inverted-band semiconductors. Phys. Rev. B *105*, 035305. https://doi.org/10.1103/PhysRevB.105.035305.
17. Grazianetti, C., and Molle, A. (2019). Engineering Epitaxial Silicene on Functional Substrates for Nanotechnology. Research *2019*, 8494606–8494608. https://doi.org/10.34133/2019/8494606.
18. Cardona, M. (1967). Band structure of gray tin under uniaxial stress. Solid State Commun. *5*, 233–235. https://doi.org/10.1016/0038-1098(67)90263-3.
19. Xu, C.-Z., Chan, Y.-H., Chen, Y., Chen, P., Wang, X., Dejoie, C., Wong, M.-H., Hlevyack, J.A., Ryu, H., Kee, H.-Y., et al. (2017). Elemental Topological Dirac Semimetal: α-Sn on InSb(111). Phys. Rev. Lett. *118*, 146402. https://doi.org/10.1103/PhysRevLett.118.146402.
20. Carrasco, R.A., Zamarripa, C.M., Zollner, S., Menéndez, J., Chastang, S. A., Duan, J., Grzybowski, G.J., Claflin, B.B., and Kiefer, A.M. (2018). The direct bandgap of gray α-tin investigated by infrared ellipsometry. Appl. Phys. Lett. *113*, 232104. https://doi.org/10.1063/1.5053884.
21. Vail, O., Taylor, P., Folkes, P., Nichols, B., Haidet, B., Mukherjee, K., and de Coster, G. (2020). Growth and Magnetotransport in Thin-Film α-Sn on CdTe. Phys. Status Solidi *257*, 1–7. https://doi.org/10.1002/pssb.201800513.
22. Thewlis, J., and Davey, A.R. (1954). Thermal Expansion of Grey Tin. Nature *174*, 1011. https://doi.org/10.1038/1741011a0.

23. Hellwege, K.-H., and Madelung, O. (1982). Landolt-Börnstein: Numerical Data and Functional Relationships in Science and Technology, New Series, Group III, *Vol. 17* (Berlin: Springer).
24. Birner, S., Zibold, T., Andlauer, T., Kubis, T., Sabathil, M., Trellakis, A., and Vogl, P. (2007). nextnano: General Purpose 3-D Simulations. IEEE Trans. Electron. Dev. *54*, 2137–2142. https://doi.org/10.1109/TED.2007.902871.
25. Xu, C.-Z., Chan, Y.-H., Chen, P., Wang, X., Flötotto, D., Hlevyack, J.A., Bian, G., Mo, S.-K., Chou, M.-Y., and Chiang, T.-C. (2018). Gapped electronic structure of epitaxial stanene on InSb(111). Phys. Rev. B *97*, 035122. https://doi.org/10.1103/PhysRevB.97.035122.
26. Vogel, A.T., de Boor, J., Becker, M., Wittemann, J.V., Mensah, S.L., Werner, P., and Schmidt, V. (2011). Ag-assisted CBE growth of ordered InSb nanowire arrays. Nanotechnology *22*, 015605. https://doi.org/10.1088/0957-4484/22/1/015605.
27. Buchenauer, C.J., Cardona, M., and Pollak, F.H. (1971). Raman Scattering in Gray Tin. Phys. Rev. B *3*, 1243–1244. https://doi.org/10.1103/PhysRevB.3.1243.
28. Oszwałldowski, M., and Zimpel, M. (1988). Temperature dependence of intrinsic carrier concentration and density of states effective mass of heavy holes in InSb. J. Phys. Chem. Solid. *49*, 1179–1185. https://doi.org/10.1016/0022-3697(88)90173-4.
29. Singh, S., Kumar, N., Roychowdhury, S., Shekhar, C., and Felser, C. (2022). Anisotropic large diamagnetism in Dirac semimetals $ZrTe_5$ and $HfTe_5$. J. Phys. Condens. Matter *34*, 225802. https://doi.org/10.1088/1361-648X/ac5d19.
30. Tang, F., Wang, P., Wang, P., Gan, Y., Wang, L., Zhang, W., and Zhang, L. (2018). Multi-carrier transport in $ZrTe_5$ film. Chin. Phys. B *27*, 087307. https://doi.org/10.1088/1674-1056/27/8/087307.
31. Ding, Y., Yao, J., Yuan, Z., Li, C., Lu, M.-H., Lu, H., and Chen, Y.-F. (2021). Multiple carrier transport in high-quality α-Sn films grown on CdTe (001) by molecular beam epitaxy. J. Vac. Sci. Technol. A *39*, 033408. https://doi.org/10.1116/6.0000756.
32. Hoffman, C.A., Meyer, J.R., Wagner, R.J., Bartoli, F.J., Engelhardt, M.A., and Höchst, H. (1989). Three-band transport and cyclotron resonance in α-Sn and α-$Sn_{1-x}Ge_x$ grown by molecular-beam epitaxy. Phys. Rev. B *40*, 11693–11700. https://doi.org/10.1103/PhysRevB.40.11693.
33. Ding, J., Liu, C., Kalappattil, V., Zhang, Y., Mosendz, O., Erugu, U., Yu, R., Tian, J., DeMann, A., Field, S.B., et al. (2021). Switching of a Magnet by Spin-Orbit Torque from a Topological Dirac Semimetal. Adv. Mater. *33*, 2005909.
34. Zollner, S. (2024). Excitonic effects in the optical absorption of gapless semiconductor α-tin near the direct bandgap. J. Vac. Sci. Technol. B *42*, 022203. https://doi.org/10.1116/6.0003278.
35. Tu, L.W., Wong, G.K., and Ketterson, J.B. (1989). Observation of quantum size effect in the resistivity of thin, gray tin epilayers. Appl. Phys. Lett. *55*, 1327–1329.
36. Ashcroft, N.W., and Mermin, N.D. (1976). Solid state physics (Dorothy Garbose Crane) LK - https://worldcat.org/title/934604.
37. Das Sarma, S., Hwang, E.H., and Min, H. (2015). Carrier screening, transport, and relaxation in three-dimensional Dirac semimetals. Phys. Rev. B *91*, 035201. https://doi.org/10.1103/PhysRevB.91.035201.
38. Hwang, E.H., and Das Sarma, S. (2008). Acoustic phonon scattering limited carrier mobility in two-dimensional extrinsic graphene. Phys. Rev. B *77*, 115449. https://doi.org/10.1103/PhysRevB.77.115449.
39. de Coster, G.J., Folkes, P.A., Taylor, P.J., and Vail, O.A. (2018). Effects of orientation and strain on the topological characteristics of CdTe/α-Sn quantum wells. Phys. Rev. B *98*, 115153. https://doi.org/10.1103/PhysRevB.98.115153.
40. Booth, B.L., and Ewald, A.W. (1968). Anisotropy of the gray-tin γ8+ conduction band. Phys. Rev. *168*, 805–811. https://doi.org/10.1103/PhysRev.168.805.
41. Merkt, U., Horst, M., Evelbauer, T., and Kotthaus, J.P. (1986). Cyclotron and spin resonance in electron inversion layers on InSb. Phys. Rev. B *34*, 7234–7245. https://doi.org/10.1103/PhysRevB.34.7234.
42. Yu, P.Y., and Cardona, M. (1996). Effect of Quantum Confinement on Electrons and Phonons in Semiconductors. In Fundamentals of Semiconductors: Physics and Materials Properties, P.Y. Yu and M. Cardona, eds. (Springer Berlin Heidelberg), pp. 469–551. https://doi.org/10.1007/3-540-26475-2_9.
43. Mohelský, I., Dubroka, A., Wyzula, J., Slobodeniuk, A., Martinez, G., Krupko, Y., Piot, B.A., Caha, O., Humlíček, J., Bauer, G., et al. (2020). Landau level spectroscopy of Bi_2Te_3. Phys. Rev. B *102*, 085201. https://doi.org/10.1103/PhysRevB.102.085201.
44. Palik, E.D., Picus, G.S., Teitler, S., and Wallis, R.F. (1961). Infrared Cyclotron Resonance in InSb. Phys. Rev. *122*, 475–481. https://doi.org/10.1103/PhysRev.122.475.
45. McCombe, B.D., and Kaplan, R. (1968). Effects of Electron-Optical-Phonon Interaction in the Combined Resonance Spectra of InSb. Phys. Rev. Lett. *21*, 756–759. https://doi.org/10.1103/PhysRevLett.21.756.
46. Jackson, J.D. (1999). Classical Electrodynamics (Wiley)).
47. Bechstedt, F., Gori, P., and Pulci, O. (2021). Beyond graphene: Clean, hydrogenated and halogenated silicene, germanene, stanene, and plumbene. Prog. Surf. Sci. *96*, 100615. https://doi.org/10.1016/j.progsurf.2021.100615.
48. Wojtowicz, T., Dobrowolska, M., Yang, G., Luo, H., Furdyna, J.K., Tu, L. W., and Wong, G.K. (1990). Far-infrared determination of cyclotron and plasma-shifted cyclotron resonances in thin MBE-grown films of α-Sn. Semicond. Sci. Technol. *5*, S248–S252. https://doi.org/10.1088/0268-1242/5/3S/054.
49. Song, S.N., Yi, X.J., Zheng, J.Q., Zhao, Z., Tu, L.W., Wong, G.K., and Ketterson, J.B. (1990). Dimensional crossover of Shubnikov-de Haas oscillations in thin films of gray tin. Phys. Rev. Lett. *65*, 227–230. https://doi.org/10.1103/PhysRevLett.65.227.
50. Ding, Y., Song, H., Huang, J., Yao, J., Gu, Y., Wei, L., Chen, Y.B., Deng, Y., Yuan, H., Lu, H., and Chen, Y.F. (2022). Wafer-Scale and Topologically Nontrivial α-Sn Films Grown on InSb(001) by Molecular-Beam Epitaxy. Phys. Rev. Appl. *17*, 014015. https://doi.org/10.1103/PhysRevApplied.17.014015.
51. Ekenberg, U. (1989). Nonparabolicity effects in a quantum well: Sublevel shift, parallel mass, and Landau levels. Phys. Rev. B *40*, 7714–7726. https://doi.org/10.1103/PhysRevB.40.7714.
52. Bastard, G. (1982). Theoretical investigations of superlattice band structure in the envelope-function approximation. Phys. Rev. B *25*, 7584–7597. https://doi.org/10.1103/PhysRevB.25.7584.
53. Wang, Z., Weng, H., Wu, Q., Dai, X., and Fang, Z. (2013). Three-dimensional Dirac semimetal and quantum transport in Cd_3As_2. Phys. Rev. B *88*, 125427. https://doi.org/10.1103/PhysRevB.88.125427.
54. Xiao, X., Yang, S.A., Liu, Z., Li, H., and Zhou, G. (2015). Anisotropic quantum confinement effect and electric control of surface states in Dirac semimetal nanostructures. Sci. Rep. *5*, 7898. https://doi.org/10.1038/srep07898.
55. Uchida, M., Nakazawa, Y., Nishihaya, S., Akiba, K., Kriener, M., Kozuka, Y., Miyake, A., Taguchi, Y., Tokunaga, M., Nagaosa, N., et al. (2017). Quantum Hall states observed in thin films of Dirac semimetal Cd_3As_2. Nat. Commun. *8*, 2274. https://doi.org/10.1038/s41467-017-02423-1.
56. Xiong, J., Kushwaha, S., Krizan, J., Liang, T., Cava, R.J., and Ong, N.P. (2016). Anomalous conductivity tensor in the Dirac semimetal Na_3Bi. Europhys. Lett. *114*, 27002. https://doi.org/10.1209/0295-5075/114/27002.
57. Hu, Z., Koo, J., Hu, Y., Wang, Q., Abeykoon, M., Graf, D., Liu, Y., Lei, H., Ma, J., Shi, M., et al. (2023). Topological Dirac semimetal BaAuSb. Phys. Rev. Res. *5*, 013079. https://doi.org/10.1103/PhysRevResearch.5.013079.